arXiv:1403.6587v1 [physics.comp-ph] 26 Mar 2014

Manuscript submitted to
AIMS' Journals
Volume **X**, Number **0X**, XX **200X**

doi:10.3934/xx.xx.xx.xx

pp. **X–XX**

ESTIMATION OF CONDUCTIVITY CHANGES IN A REGION OF INTEREST WITH ELECTRICAL IMPEDANCE TOMOGRAPHY

Dong liu and Ville Kolehmainen

Department of Applied Physics, University of Eastern Finland, FIN-70211 Kuopio, Finland

Samuli Siltanen

Department of Mathematics and Statistics, University of Helsinki, FIN-00014 Helsinki, Finland

Anne-maria Laukkanen

School of Education, University of Tampere, FIN-33014 Tampere, Finland

Aku Seppänen

Department of Applied Physics, University of Eastern Finland, FIN-70211 Kuopio, Finland

(Communicated by the associate editor name)

Abstract. This paper proposes a novel approach to reconstruct changes in a target conductivity from electrical impedance tomography measurements. As in the conventional *difference imaging*, the reconstruction of the conductivity change is based on electrical potential measurements from the exterior boundary of the target before and after the change. In this paper, however, images of the conductivity before and after the change are reconstructed simultaneously based on the two data sets. The key feature of the approach is that the conductivity after the change is parameterized as a linear combination of the initial state and the change. This allows for modeling independently the spatial characteristics of the background conductivity and the change of the conductivity - by separate regularization functionals. The approach also allows in a straightforward way the restriction of the conductivity change to a localized region of interest inside the domain. While conventional difference imaging reconstruction is based on a global linearization of the observation model, the proposed approach amounts to solving a non-linear inverse problem. The feasibility of the proposed reconstruction method is tested experimentally and with a simulation which demonstrates a potential new medical application of electrical impedance tomography: imaging of vocal folds in voice loading studies.

1. **Introduction.** In electrical impedance tomography (EIT), electrical currents are injected into an object using a set of electrodes attached on the boundary of the object and the resulting electrode potentials are measured. The conductivity of the object is reconstructed as a spatially distributed parameter based on the known

2010 *Mathematics Subject Classification.* Primary: 58F15, 58F17; Secondary: 53C35.

Key words and phrases. Inverse problem, electrical impedance tomography, absolute imaging, region of interest, imaging of vocal folds.

This work was supported by the Academy of Finland under projects 119270, 134868, 140280, 250215 and 270174, Finnish Doctoral Programme in Computational Sciences and Finnish Center of Excellence of Inverse Problems Research 2012-2017.

currents and measured potentials. EIT has been applied to e.g. geophysical exploration [11], biomedical imaging [18, 8, 64, 3, 57, 1], industrial process monitoring and control [52] and non-destructive testing [23, 24, 32, 31]. For reviews of EIT, see [6, 28, 5, 22, 43].

The EIT image reconstruction problem is an ill-posed inverse problem. The generalized Tikhonov regularization framework [58] is often used in practical applications. Other options within the deterministic inversion framework include variational regularization with sparsity constraints [27] and direct methods, such as the D-bar method [55, 25, 26, 33]; see also [43, Table 14.1]. For Bayesian approaches, see [28, 30]. Reconstructing the distributed conductivity by solving the non-linear inverse problem of EIT is referred to as *absolute imaging* [60, 64].

Many applications of EIT aim at monitoring a time-varying object. Often the main interest is to track *changes* in the conductivity between two measurements, rather than estimate absolute conductivity values. In *difference imaging* [6, 57, 5, 1, 18, 61, 9], the conductivity change is estimated based on difference data, i.e. difference between the electrode potentials before and after the change. A conventional approach to image reconstruction in difference imaging is to linearize the mapping between the electrical conductivity and the electrode potentials globally at some *a priori* defined conductivity, and to solve a linear inverse problem such as a regularized linear least squares problem. Due to the linearization, the images are often only qualitative in nature and their spatial resolution may be low, especially if the target conductivity is highly inhomogeneous before and/or after the change.

We note that some exceptions to linearization-based approach exist: the D-bar method can be used for both absolute and difference imaging [25, 26] without linearizing the model. In the present paper, we formulate the reconstruction problem in the generalized Tikhonov regularization framework. Also in the proposed reconstruction method, the global linearization of the model is not needed. We also note that the proposed method could be formulated equivalently in the Bayesian inversion framework.

The conventional linearization-based reconstruction approach is widely used in difference imaging, especially because the reconstructions are fast to compute, and because the reconstructions are to some extent tolerant of modeling errors because of the partial cancellation of the errors in the subtraction of the measurement data from the data after the change. Typical sources of modeling errors in EIT are the unknown shape of the body, inaccurately known electrode positions and unknown contact impedances between the electrodes and the body surface. If these uncertainties are not accounted for, the solutions of the non-linear absolute imaging problem can be highly erroneous, due to the ill-posedness of the inverse problem. However, if all model uncertainties are modeled properly, the absolute imaging can give quantitative information on the tissue properties. Recently, several approaches for handling the above uncertainties and other model inaccuracies have been developed. For the recovery from unknown boundary shape and/or electrode locations, alternative approaches have been proposed [35, 36, 37, 46, 45, 4, 12, 13, 14]. All these reconstruction methods have also been evaluated with real measurement data [37, 46, 4, 14]. For two alternative computational methods for recovering from unknown contact impedances in absolute imaging, see [62, 44]. In the latter paper, also modeling errors due to discretization and domain truncation were accounted for, by using the so-called approximation error method.

If the application at hand does not require real-time imaging and if quantitative information is desired, a preferable choice is to handle the model uncertainties properly and to compute solution to the non-linear problem instead of using the linearization based approach. However, when the measurement data of the target before and after the change are available, it might be possible to somehow combine the data sets within the absolute EIT imaging framework. Our hypothesis is that this could improve the quality of the absolute EIT reconstructions, especially if the change of the conductivity is known to be restricted to a subvolume (region of interest, ROI) inside the body. Examples of such applications are monitoring of water ingress in soil [11] and cracking of concrete [24, 31], assessment of regional lung ventilation [61, 41, 10, 39, 49] and monitoring of intraperitoneal bleeding [63]. This is also the case in a potential new application of EIT: imaging of vocal folds in voice loading studies [34, 53, 21, 42]. Indeed, the location of the glottis is known relatively well, and vocal folds are the most rapidly moving part in a human body; hence, during the movement of vocal folds, the conductivity changes outside a relatively small volume around the glottis are negligible.

In this paper, we formulate the non-linear reconstruction problem for a temporally varying target so that the measurements before and after the target change are concatenated into single measurement vector, and the two conductivity distributions are reconstructed simultaneously based on the combined data. The key feature in the approach is that conductivity after the change is represented as a linear combination of the initial state and the change of the conductivity. This allows for modeling separately the spatial characteristics of the background conductivity and the change of the conductivity - by separate regularization functionals. This also enables the restriction of the conductivity change to a region of interest.

The rest of this paper is organized as follows. In Section 2, a brief review of the EIT observation model is given, and the properties of the absolute and difference imaging are outlined. In Section 3, the new approach for reconstructing changes in the region of interest is proposed. The proposed approach is tested with experiments in Section 4 and with a simulation related to glottis imaging application in Section 5. Conclusions are drawn in Section 6.

2. Absolute and difference imaging in EIT.

2.1. Forward Model.

Let $\Omega \subset \mathbb{R}^q, q = 2, 3$ denote the body to be imaged. In EIT, L contact electrodes are attached to the positions $e_\ell \subset \partial\Omega \;\; \ell = 1, 2, \ldots, L$ on the boundary $\partial\Omega$. Electric currents are injected into the body using the electrodes, and the resulting electrode potentials are measured. These measurements may consist of potential differences (voltages) between a set of electrode pairs, or potentials of the electrodes with respect to a common ground.

The most accurate physically realizable model for such measurements is referred to as the complete electrode model [7]

$$\nabla \cdot (\sigma(x)\nabla u(x)) = 0 \ , \ x \in \Omega \tag{1}$$

$$u(x) + z_\ell \sigma(x) \frac{\partial u(x)}{\partial n} = U_\ell, \ x \in e_\ell, \ \ell = 1, ..., L \tag{2}$$

$$\int_{e_\ell} \sigma(x) \frac{\partial u(x)}{\partial n} \, \mathrm{d}S = I_\ell, \quad \ell = 1, ..., L \tag{3}$$

$$\sigma(x) \frac{\partial u(x)}{\partial n} = 0, \quad x \in \partial\Omega \backslash \bigcup_{\ell=1}^{L} e_\ell \tag{4}$$

where $x \in \Omega$ is the spatial coordinate, $\sigma(x)$ is the conductivity, $u(x)$ is the electric potential distribution inside Ω, U_ℓ and I_ℓ are the potential and current at electrode ℓ, respectively, z_ℓ is the contact impedance between the electrode e_ℓ and the body Ω, and n denotes the outward unit normal vector on the boundary $\partial\Omega$. The currents satisfy the charge conservation law

$$\sum_{\ell=1}^{L} I_\ell = 0, \tag{5}$$

and a ground level for the potentials needs to be fixed, for example by writing

$$\sum_{\ell=1}^{L} U_\ell = 0. \tag{6}$$

The existence and uniqueness of the solution of the model (1-6) was proven and its weak form written in [56]. For the *finite element* (FE) approximation of the model, see [60].

Assuming an additive Gaussian noise model, the FE approximation of (1-6) leads to the observation model

$$V = U(\sigma) + e \tag{7}$$

where $V \in \mathbb{R}^M$ is the vector including all the measured electrode potentials. Here, $M = mN_{\text{inj}}$, where N_{inj} denotes the number of current injections and m is the number of measured potentials or voltages for each current injection. Further, U is the mapping between the finite dimensional approximation of the conductivity σ and the electrode potentials, and $e \in \mathbb{R}^M$ is the Gaussian distributed measurement noise $e \sim \mathcal{N}(e^*, \Gamma_e)$. The mean $e^* \in \mathbb{R}^M$ and the covariance matrix $\Gamma_e \in \mathbb{R}^{M \times M}$ can usually be determined experimentally, see [20].

2.2. **Absolute imaging.** In absolute imaging, the conductivity σ is reconstructed using a single set of potential measurements V during which the target is assumed to be non-varying.

Within the *generalized Tikhonov regularization* framework, the estimate for the conductivity is obtained as

$$\hat{\sigma} = \arg\min_{\sigma > 0} \{ \|L_e(V - U(\sigma))\|^2 + p_\sigma(\sigma) \} \tag{8}$$

where L_e is a Cholesky factor of the noise precision matrix, i.e. $L_e^{\mathrm{T}} L_e = \Gamma_e^{-1}$, and $p_\sigma(\sigma)$ is a regularization functional. The functional $p_\sigma(\sigma)$ is usually designed such that it gives high penalty for unwanted/improbable features of σ. Examples of widely used regularization functionals are smoothness regularization $p_\sigma(\sigma) = \|L\sigma\|^2$ where $L\sigma$ is some (possibly spatially and directionally weighted) differential of the

conductivity [48, 30, 29] and total variation (TV) regularization $p_\sigma(\sigma) = \alpha\|\nabla\sigma\|_1$ [51, 15, 28]. For example, targets that are results of diffusion processes, are usually modeled with a (homogeneous) smoothness regularization, while piecewise regular targets which have sparse gradient image might be modeled with a TV prior model.

We note that the estimate (8) can be intepreted in the Bayesian inversion framework as the maximum a posteriori (MAP) estimate from a posterior density model which is based on the observation model (7) and a Gibbs type prior model with prior potential (or functional) $p_\sigma(\sigma)$, see [30].

The minimization problem (8) can be solved iteratively, for example with the Gauss-Newton method while the positivity constraint on the conductivity can be taken into account by using interior point methods [16, 47]. For properties of different optimization methods in EIT, see e.g. [59].

2.3. **Difference imaging.** Consider two EIT measurement realizations V_1 and V_2 at time instants t_1 and t_2, corresponding to conductivities σ_1 and σ_2, respectively. The observation models corresponding to the two EIT measurement realizations can be written as in Equation (7)

$$V_1 = U(\sigma_1) + e_1 \tag{9}$$

$$V_2 = U(\sigma_2) + e_2 \tag{10}$$

where $e_i \sim \mathcal{N}(e^*, \Gamma_e)$, $i = 1, 2$. The aim in difference imaging is to reconstruct the change in conductivity $\delta\sigma = \sigma_2 - \sigma_1$ based on the change $\delta V = V_2 - V_1$ in the data.

Conventionally, the image reconstruction in difference imaging is carried out as follows. Models (9) and (10) are approximated by first order Taylor approximations as:

$$V_i \approx U(\sigma_0) + J(\sigma_i - \sigma_0) + e_i, \qquad i = 1, 2 \tag{11}$$

where σ_0 is the linearization point, and $J = \frac{\partial U}{\partial \sigma}(\sigma_0)$ is the Jacobian matrix evaluated at σ_0. Using the linearizations and subtracting V_1 from V_2 gives the *linear* observation model

$$\delta V \approx J\delta\sigma + \delta e \tag{12}$$

where $\delta V = V_2 - V_1$, $\delta\sigma = \sigma_2 - \sigma_1$ and $\delta e = e_2 - e_1$.

Given the model (12), the conductivity change $\delta\sigma$ can be reconstructed as

$$\widehat{\delta\sigma} = \arg\min_{\delta\sigma}\{\|L_{\delta e}(\delta V - J\delta\sigma)\|^2 + p_{\delta\sigma}(\delta\sigma)\} \tag{13}$$

where $p_{\delta\sigma}(\delta\sigma)$ is a regularization functional. The weighting matrix $L_{\delta e}$ is defined as $L_{\delta e}^{\mathrm{T}} L_{\delta e} = \Gamma_{\delta e}^{-1}$, where $\Gamma_{\delta e}$, the covariance of the noise term δe is $\Gamma_{\delta e} = \Gamma_{e_1} + \Gamma_{e_2} = 2\Gamma_e$.

Note that the regularization functional $p_{\delta\sigma}(\delta\sigma)$ is often chosen to be of the quadratic form $p_{\delta\sigma}(\delta\sigma) = \|L_{\delta\sigma}\delta\sigma\|^2$ where $L_{\delta\sigma}$ is a *regularization matrix*. In such a case, (13) is of the form of a regularized linear least squares problem, the solution of which can be computed with one step – in contrast to iterative solution of (8) in absolute imaging. The main benefit of the difference imaging, however, is that when considering the difference data δV at least part of the systematic errors in the models/measurements are subtracted, and hence the estimates are often to some extent tolerant of systematic measurement errors and model uncertainties and inaccuracies. A drawback of the approach is that the difference images are usually only qualitative in nature and their spatial resolution can be weak, because they rely on the global linearization of the non-linear observation model (7). Moreover, the estimates depend on the selection of the linearization point σ_0. Typically, σ_0 is

selected as a homogeneous (spatially constant) estimate of the initial conductivity σ_1. This choice can lead to significant errors in the reconstructions, especially if the initial conductivity is highly inhomogeneous.

3. **Absolute imaging of the conductivity change in a region-of-interest.** In this section, we formulate the reconstruction of the conductivity change in the absolute imaging framework, in the case where two measurements V_1 and V_2, taken before and after the change of target, are available. Instead of considering the obvious approach of reconstructing σ_1 and σ_2 by solving minimization (8) *separately* for realizations $V_i,\ i = 1, 2$ and then subtracting $\delta\sigma = \sigma_2 - \sigma_1$, we propose an approach where $\delta\sigma$ is reconstructed together with σ_1 by using simultaneously measurements V_1 and V_2. With this approach, we gain flexibility for modeling prior information in cases where i) the spatial characteristics of initial state σ_1 and the change $\delta\sigma$ are different (for example, smooth σ_1 but sparse $\delta\sigma$) and/or ii) the change in the conductivity is known to be restricted to a localized subvolume (region of interest, ROI) of the body Ω. Utilizing such prior information is expected to improve the accuracy of the EIT reconstructions.

The observation models for the two EIT data sets V_1 and V_2 are of the forms (9-10). Assume that the conductivity change $\delta\sigma = \sigma_2 - \sigma_1$ is known to be restricted to a region of interest $\Omega_{\text{ROI}} \subseteq \Omega$, and denote the conductivity change within Ω_{ROI} by $\delta\sigma_{\text{ROI}}$. Then, $\delta\sigma = \mathcal{M}\delta\sigma_{\text{ROI}}$ where $\mathcal{M}$ is the mapping $\mathcal{M} : \Omega_{\text{ROI}} \to \Omega$ such that

$$\mathcal{M}\delta\sigma_{\text{ROI}} = \begin{cases} \delta\sigma_{\text{ROI}}, & x \in \Omega_{\text{ROI}} \\ 0, & x \in \Omega \setminus \Omega_{\text{ROI}} \end{cases} \tag{14}$$

and σ_2, the conductivity after the change, can be represented in the form

$$\sigma_2 = \sigma_1 + \mathcal{M}\delta\sigma_{\text{ROI}}. \tag{15}$$

Inserting expression (15) to Equation (10) and concatenating the measurement vectors V_1 and V_2 and the corresponding models in (9-10) into block vectors leads to observation model

$$\underbrace{\begin{bmatrix} V_1 \\ V_2 \end{bmatrix}}_{\bar{V}} = \underbrace{\begin{bmatrix} U(\sigma_1) \\ U(\sigma_1 + \mathcal{M}\delta\sigma_{\text{ROI}}) \end{bmatrix}}_{\bar{U}(\bar{\sigma})} + \underbrace{\begin{bmatrix} e_1 \\ e_2 \end{bmatrix}}_{\bar{e}} \tag{16}$$

or

$$\bar{V} = \bar{U}(\bar{\sigma}) + \bar{e}, \tag{17}$$

where

$$\bar{\sigma} = \begin{bmatrix} \sigma_1 \\ \delta\sigma_{\text{ROI}} \end{bmatrix}.$$

Here, we have identified the conductivities $\sigma_1, \delta\sigma_{\text{ROI}}$ and mapping $\mathcal{M}$ with their finite dimensional approximations.

Based on the observation model (17), the generalized Tikhonov regularized solution is written in the form

$$\hat{\bar{\sigma}} = \arg\min_{\bar{\sigma}} \{ \|L_{\bar{e}}(\bar{V} - \bar{U}(\bar{\sigma}))\|^2 + p_{\bar{\sigma}}(\bar{\sigma}) \}. \tag{18}$$

Here, $L_{\bar{e}} \in \mathbb{R}^{2M \times 2M}$ is the Cholesky factor such that $L_{\bar{e}}^{\mathrm{T}} L_{\bar{e}} = \Gamma_{\bar{e}}^{-1}$, where

$$\Gamma_{\bar{e}} = \begin{bmatrix} \Gamma_{e_1} & \mathbf{0}_{M \times M} \\ \mathbf{0}_{M \times M} & \Gamma_{e_2} \end{bmatrix}$$

and $\mathbf{0}_{M\times M} \in \mathbb{R}^{M\times M}$ is an all-zero matrix. Typically, the noise statistics can be modelled stationary, i.e., $\Gamma_{e_1} = \Gamma_{e_2} = \Gamma_e$. Further, $p_{\bar\sigma}(\bar\sigma)$ is a compound regularization functional of the form

$$p_{\bar\sigma}(\bar\sigma) = p_{\sigma_1}(\sigma_1) + p_{\delta\sigma_{\mathrm{ROI}}}(\delta\sigma_{\mathrm{ROI}})$$

which allows naturally the use of different spatial models for σ_1 and $\delta\sigma$. Similarly as in Section 2.2, the Tikhonov regularized solution (18) has to be computed iteratively. In the iterations, the Jacobian matrix $J_{\bar U}(\bar\sigma) = \frac{\partial \bar U}{\partial \bar\sigma}$ is needed; the Jacobian is of the form

$$J_{\bar U}(\bar\sigma) = \begin{bmatrix} J_U(\sigma_1) & \mathbf{0}_{M\times N_{\mathrm{ROI}}} \\ J_U(\sigma_1 + \mathcal{M}\delta\sigma_{\mathrm{ROI}}) & J_U(\sigma_1 + \mathcal{M}\delta\sigma_{\mathrm{ROI}})\mathcal{M} \end{bmatrix}$$

where $J_U(\sigma)$ is the Jacobian matrix of the function $U(\sigma)$, $\mathbf{0}_{M\times N_{\mathrm{ROI}}} \in \mathbb{R}^{M\times N_{\mathrm{ROI}}}$ is an all-zero matrix, and N_{ROI} is the dimension of the vector $\delta\sigma_{\mathrm{ROI}}$.

In contrast to conventional difference imaging reconstruction (Section 2.3), the global linearization of the EIT forward model is *not* needed here, enabling the use of the two data realizations for quantitative imaging. This of course necessitates that (possible) modeling errors are handled properly, see Section 1 and the references therein. Moreover, utilizing the information on the approximate position of the conductivity change between the two measurement sets V_1 and V_2 is expected to improve the reconstructions, especially if the ROI is relatively small in comparison with the volume of the target. Note also that the two regularization terms $p_{\sigma_1}(\sigma_1)$ and $p_{\delta\sigma_{\mathrm{ROI}}}(\delta\sigma_{\mathrm{ROI}})$ corresponding to σ_1 and $\delta\sigma_{\mathrm{ROI}}$, respectively, may have different properties. In the examples shown in the following sections, $p_{\sigma_1}(\sigma_1)$ corresponds to the assumption of a smooth initial conductivity σ_1, while $p_{\delta\sigma}(\delta\sigma)$ corresponds to a total variation (TV) model for the conductivity change.

Finally, we note that an alternative approach to non-stationary imaging is the state-estimation, in which Kalman filter -type recursive estimators are used for reconstructing the time-varying conductivity distribution. The state-estimation approach has shown to be beneficial when the measurements are obtained sequentially and feasible models for the target evolution are available – such as fluid dynamical models in industrial process imaging applications [54]. In principle, the region-of-interest information utilized in the present study could be utilized in the state-estimation equivalently. The implementation of the TV regularization used in this paper for the conductivity change, however, would not be a straightforward task in the state-estimation framework.

4. Experimental studies.

The feasibility of the proposed reconstruction method was studied experimentally. All tests were carried out with targets that were translationally symmetric in the vertical direction, and hence two-dimensional models were adequate for modeling the measurements. The extension of the computational methods to a purely three-dimensional case is straightforward.

4.1. Experimental setup.

The experiments were carried out using a cylindrical tank shown in fig. 1 in the top row. The diameter of the tank was 28 cm. Sixteen equally spaced metallic electrodes (width 2.5 cm, height 7.0 cm) were attached to the inner surface of the tank. In fig. 1, the electrode positions are indicated with red stripes on the tank boundary. The rightmost electrode was identified with electrode index $\ell = 1$, and the electrode indices increased in counter clockwise direction. The tank was filled with saline, and plastic objects with different shapes were placed in the tank to form inhomogeneities to the conductivity distribution.

The EIT measurements were carried out with KIT4 measurement system developed in the Department of Applied Physics, University of Eastern Finland [38]. Pairwise current injections were applied in the measurements. The frequency of the current was 1 kHz and the amplitude was 1 mA. The currents were injected such that one electrode was fixed as the sink electrode and then applying pairwise currents sequentally between the sink electrode and each one of the 15 remaining electrodes. This process was repeated using electrodes $\{1, 5, 9, 13\}$ as the sink, leading to total of 54 current injections when reciprocal curret injections were not taken. Corresponding to each current injection, the potentials on all the 15 remaining electrodes were measured against the sink electrode, which was connected to the common ground. With this measurement protocol, one measurement frame consists of 810 voltage readings (i.e., $V \in \mathbb{R}^{810}$).

Three different experimental test cases were considered. In all cases, two realizations of EIT measurements were collected: V_1 corresponding to an initial conductivity σ_1 and V_2 corresponding to conductivity σ_2 after a change. The first test case is illustrated in fig. 1. In the initial state σ_1 (top left), a plastic circular cylinder (diameter 6.2 cm) was placed in the tank. In the second state σ_2 (top middle), a plastic triangular prism was added to the tank. The top face of the prism was an equilateral triangle, and the edges of the triangle were 8.5 cm long. In test cases 2 and 3, three plastic cylindrical objects were placed in the tank in the initial state σ_1 (figs. 2 and 3, top left). In both cases, a tetragonal prism was added to the tank in the second state σ_2. The difference between cases 2 and 3 was that sizes of the inserted tetragonal prisms were different: in case 2, the dimensions of the prism face were 8.2 cm $\times$ 3.5 cm (fig. 2, top middle) and in case 3, 6.0 cm $\times$ 1.0 cm (fig. 3, top middle).

To estimate the noise level, we carried repeated measurement (100 realizations) from the tank filled with saline. The noise covariance matrix Γ_e was computed as a sample covariance based on these realizations.

4.2. **Estimates.** In each of the three test cases, the following estimates were computed:

(E1) Conventional (linear) difference reconstruction by solving

$$\widehat{\delta\sigma} = \arg\min_{\delta\sigma}\{\|L_{\delta e}(\delta V - J\delta\sigma)\|^2 + \|L_{\delta\sigma}\delta\sigma\|^2\}$$

where $L_{\delta\sigma}^{\mathrm{T}} L_{\delta\sigma} = \Gamma_{\delta\sigma}^{-1}$, and

$$\Gamma_f(i,j) = a \exp\left\{-\frac{\|x_i - x_j\|_2^2}{2b^2}\right\} + c\delta_{ij}. \tag{19}$$

is covariance matrix corresponding to a generic smoothness prior model for the unknown distributed parameter f [40]. Here x_i and x_j denote the coordinate points of nodes i an j in the parameterization of f, respectively.

(E2) Absolute reconstructions of σ_1 and σ_2 by solving

$$\hat{\sigma}_i = \arg\min_{\sigma_i>0}\{\|L_e(V_i - U(\sigma_i))\|^2 + \|L_{\sigma_i}(\sigma_i - \sigma^*)\|^2\}.$$

The regularization matrix $L_{\sigma_i}^{\mathrm{T}} L_{\sigma_i} = \Gamma_{\sigma_i}^{-1}$ was constructed by equation (19).

(E3) Absolute reconstructions of σ_1 and σ_2 by solving

$$\hat{\sigma}_i = \arg\min_{\sigma_i>0}\{\|L_e(V_i - U(\sigma_i))\|^2 + \alpha\mathrm{TV}(\sigma_i)\},$$

where

$$\mathrm{TV}(f) = \sum_{k=1}^{N_e} |\Omega_k| \sqrt{\|(\nabla f)|_{\Omega_k}\|^2 + \beta}$$

is a differentiable approximation of the isotropic total variation functional [51] and $(\nabla f)|_{\Omega_k}$ is the (constant) gradient of the (piecewise linear) f at element Ω_k, and N_e is the number of elements.

(E4) Reconstruction of $\bar{\sigma} = (\sigma_1^{\mathrm{T}}, \delta\sigma_{\mathrm{ROI}}^{\mathrm{T}})^{\mathrm{T}}$ with the proposed method

$$\hat{\bar{\sigma}} = \arg\min_{\bar{\sigma}} \left\{ \|L_{\bar{e}}(\bar{V} - \bar{U}(\bar{\sigma}))\|^2 + p_{\bar{\sigma}}(\bar{\sigma}) \right\}$$

$$\sigma_1 > 0, \ \sigma_1 + \mathcal{M}\delta\sigma_{\mathrm{ROI}} > 0$$

with the choice

$$p_{\bar{\sigma}}(\bar{\sigma}) = \|L_\sigma(\sigma_i - \sigma^*)\|^2 + \alpha \mathrm{TV}(\delta\sigma_{\mathrm{ROI}})$$

In all three test cases, the ROI in estimate (E4) was selected to be a circular area with a diameter 7.0 cm and a center point at (0 cm, 6 cm).

4.3. **Parameters in the reconstructions.** The contact impedances of the electrodes were estimated using data from the tank filled solely with water. Based on these measurements, we computed an estimate for the water conductivity $\sigma_0 \in \mathbb{R}$ and a constant contact impedance $z_0 \in \mathbb{R}$ as a solution of a two parameter non-linear least squares fitting problem. The estimated water conductivity was $\sigma_0 = 3.7569\mathrm{mS}$ and the estimated contact impedance was $z_0 = 1.08 \times 10^{-4}\Omega\mathrm{m}$. Note that the measurements with a homogeneous object are not a necessity for the reconstruction; for computational methods for recovering from unknown contact impedances without the additional calibration measurements, see [62, 44, 37].

In the reconstructions (E1)-(E4), the conductivity (or the change of conductivity) was approximated in a piece-wise linear first order nodal FE basis with $N_n = 1330$ nodes and $N_e = 2532$ triangular elements. Thus, the unknown conductivity vector was $\sigma \in \mathbb{R}^{1330}$. The electrical potential was approximated in a separate second order basis with 9109 nodes and 4466 elements.

The parameters a, b and c in the construction of the prior covariance (19) used in (E1), (E2) and (E4) were selected as $a = 4.53\mathrm{mS}^2$, $b = 4.61\mathrm{mS}^2$ and $c = 4.5 \times 10^{-3}\mathrm{cm}$. The expectation σ^* in (E2) and (E4) was set equivalent to the estimated saline conductivity. For interpretation of the prior covariance parameters, see e.g. [14]. The regularization parameter α for the total variation functional was selected as $\alpha = 1.30$. For the parameter β in the TV functional we used value $\beta = 1 \times 10^{-3}$.

The estimates (E2)-(E4) were computed with the Gauss-Newton optimization method which was equipped with an explicit line search algorithm. The positivity constraints were taken into account by using an interior point method where the constrained minimization problem is approximated by a sequence of unconstrained problems which use a logarithmic barrier functional for enforcing positivity of the parameters, see [16, 47]

4.4. **Results and discussion.** The results for the experimental test cases are shown in Figs 1-3. Notice that since we are employing a two-dimensional model for vertically translationally symmetric 3D objects, the conductivity values represent the product γh, where γ is the (cylindrically symmetric) three-dimensional conductivity distribution and h is the height of the cylinder. Accordingly, the contact impedance z_ℓ represents $z_\ell = \xi_\ell / h$, where ξ_ℓ is the contact impedance in a three-dimensional model.

In Figs 1-3, the first row shows photographs of the measurement tank at the initial state (conductivity σ_1) and after the change (conductivity σ_2) and the linear difference reconstruction (E1). The second row shows the reconstruction (E2), where $\hat{\sigma}_1$ and $\hat{\sigma}_2$ are computed as separate absolute reconstructions with the smoothness regularization, and the third row represents the reconstruction (E3), which is based on computing separate absolute reconstruction using the total variation regularization. In both (E2) and (E3), the estimate for the target change $\delta\sigma$ is obtained simply as $\widehat{\delta\sigma} = \hat{\sigma}_2 - \hat{\sigma}_1$. The fourth row shows the reconstruction (E4) with the proposed method. The region of interest is shown with black line in the reconstructed images. The number of nodes inside the region of interest was 320, and thus $\bar{\sigma} = (\sigma_1^{\mathrm{T}}, \delta\sigma_{\mathrm{ROI}}^{\mathrm{T}})^{\mathrm{T}} \in \mathbb{R}^{1650}$.

For quantitating the results, we computed size estimates for the inclusions in the reconstructed images of the conductivity change $\delta\sigma$. First, we estimated the areas of the inclusions in (E1)-(E4); as a threshold for the inclusion boundaries we used the mean values of the respective estimates $\widehat{\delta\sigma}$. Secondly, for test cases 2 and 3, where the true changes of the conductivities were due to inclusions with rectangular shapes, we also determined the widths of the inclusions in the reconstructions $\widehat{\delta\sigma}$. The width estimates were calculated as half widths of the inclusions along the horizontal line at distance of 5.5 cm above the center of the domain. Both the area and the width estimates and the true values are listed in Table 1.

The results of Case 1 with triangular inclusion are illustrated in Fig 1. All reconstructions methods detect the inclusion at least roughly (estimates for the conductivity change $\delta\sigma$, third column). However, the quality of the estimate (E4) obtained with the proposed method is superior to qualities of the other estimates; indeed, the triangular shape of the inclusion is tracked notably well in (E4). Moreover, Table 1 shows that the area estimate based on (E4) is closest to the true area of the triangle.

Also in Cases 2 and 3, different reconstruction methods detected the inclusions with varying accuracies. In Case 2 (Fig 2), where the rectangular inclusion was larger, the inclusion is clearly visible in all estimates for $\delta\sigma$. The size of the inclusion, however, is significantly overestimated in all reconstructions: While the true area and width of the rectangle were 28.70 cm^2 and 3.5 cm, respectively, the area estimates vary between 41.04 cm^2 and 73.69 cm^2 and the width estimates between 5.54 cm and 6.47 cm, see Table 1. The width estimate 5.54 cm closest to the true value was obtained with the proposed ROI-based reconstruction method (E4). In Case 3 (Fig 3), estimate (E4) is clearly the best one: (E4) is the only estimate showing even approximatively the elongated shape of the inclusion. Also the area and width estimates corresponding to (E4) are clearly closest to the true values. Most importantly, *(E4) is the only estimate capable for showing a clear difference between the size of the inclusion in Case 2 and that in Case 3.* Indeed, with reconstructions (E1)-(E3) the estimated widths of the inclusion in Case 3 are close to those in Case 2, but with (E4), the width estimate drops from 5.54 cm in Case 2 to 2.76 cm in Case 3.

5. **Simulation study with a larynx model.** As the last test case (Case 4), we consider a simulation study of a possible new application of EIT; imaging of the vocal folds. The conductivity changes detected by EIT could potentially be used for detecting the vocal folds movement during speech production, or estimating the

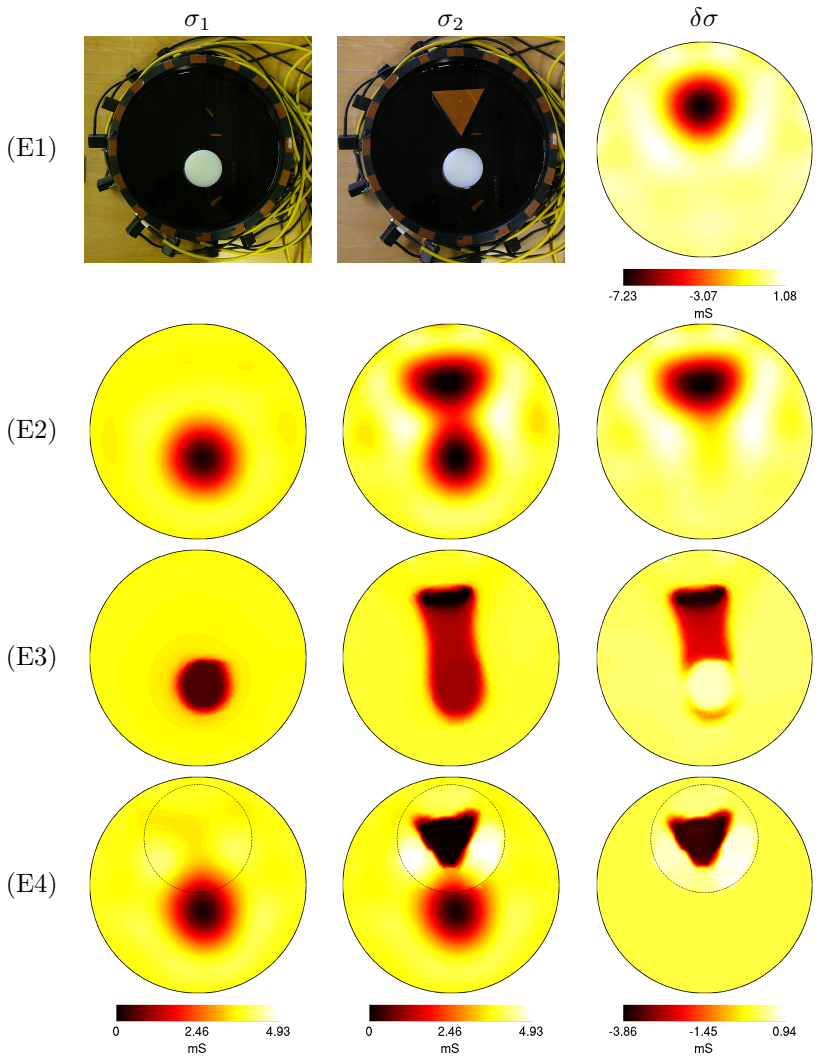

FIGURE 1. Case 1: Reconstructions from real data. (E1)-(E4) refer to the estimates listed in section 4.2.

physiological changes in the vocal fold tissue caused by vocal loading. This information could be utilized for detecting and quantifying vocal loading (i.e. getting estimates of stresses acting upon the tissue) and measuring the consequences of vocal loading (i.e. changes in the tissue). Indeed, EIT has a high potential for glottal diagnostics. Basically the data used in EIT consists of similar measurements that are also used in electroglottography (EGG) [17, 50], which is a widely used tool in the assessment of voice production. However, while in standard EGG two-channel impedance measurement data is measured for producing a (scalar valued) time serie of changes in tissue impedance, EIT is based on multi-channel data and produces tomography images of the impedance changes between the measurement frames. Recently, in [34, 21] multi-channel-EGG systems for improving the assessment of glottal opening and the laryngeal position have been proposed. In these papers, the

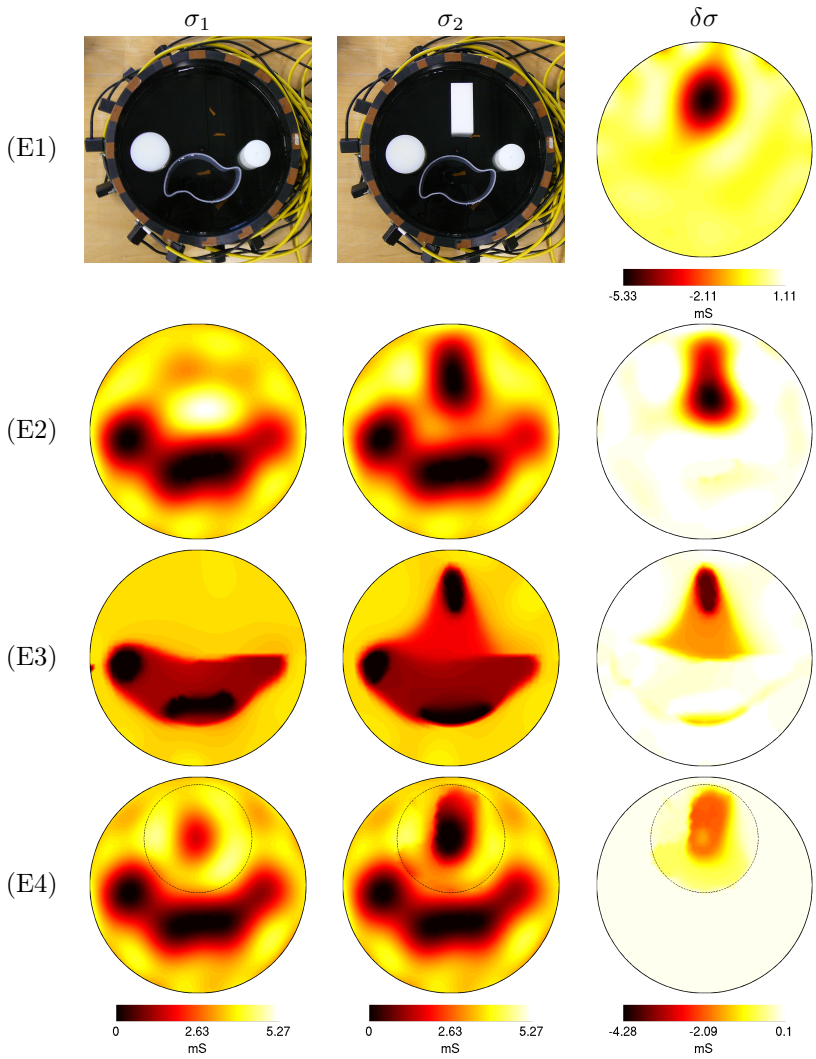

FIGURE 2. Case 2. Reconstructions from real data. (E1)-(E4) refer to the estimates listed in section 4.2.

measurement setup was similar to EIT, but the data was not used for 3D image reconstruction. However, the results in [34] indicated that it is possible to track the location of glottis during a swallowing manoeuvre.

In Fig. 4, the top row shows the true initial conductivity σ_1 (left), the conductivity after the change σ_2 (middle) and the true difference $\sigma_2 - \sigma_1$ (right). The simulation geometry was taken from a computerized tomography (CT) image of the neck area. The CT image was segmented into subdomains corresponding to bone, bone marrow, soft tissues, cartilage and trachea. The width of the neck was 11.78 cm. The conductivities of the tissues were set as 0.65 mS for bone, 4.55 mS for bone marrow, 6.5 mS for soft tissues and 7.8 mS for cartilage, corresponding to values found in the literature [19, 2]. Note, however, that in reality, i) there are more fine structures across the neck than in our model case, ii) there is some variation in the

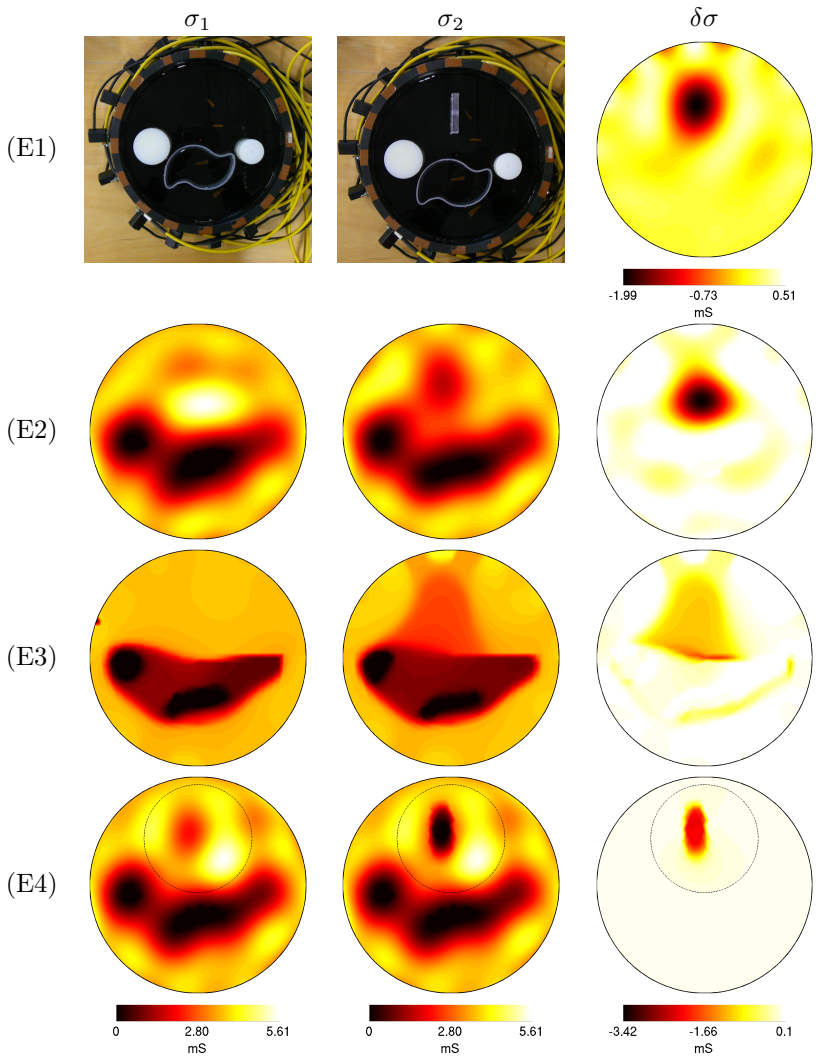

FIGURE 3. Case 3: Reconstructions from real data. (E1)-(E4) refer to the estimates listed in section 4.2.

tissue conductivity also within each organ, and iii) the target is three-dimensional. The initial state σ_1 corresponds to a case where the vocal folds are closed by holding breath. The conductivity σ_2 after the change corresponds to a case where the vocal folds are partially open, forming a thin non-conducting opening in the trachea.

In this simulation, a partial boundary measurement geometry was employed such that $L = 12$ electrodes were placed on the frontal part of the neck boundary near the glottal area, the electrode array covering less than half of the boundary $\partial\Omega$. The electrodes are illustrated with thick black lines in Fig. 4 (top left). The rightmost electrode was identified with electrode index $\ell = 1$, and the electrode indices increased in counter clockwise direction. In the simulation of the measurement data, pairwise current injections were employed such that one of the electrodes was fixed as the sink and currents were applied sequentally between the sink and each

TABLE 1. True areas and widths of the inclusions related to change of the conductivity $\delta\sigma$ (third column), and area and width estimates for the inclusions based on reconstructions (E1)-(E4).

		True	(E1)	(E2)	(E3)	(E4)
Case 1	area (cm^2)	31.29	40.44	50.37	61.56	35.44
Case 2	area (cm^2)	28.70	41.04	51.30	73.69	46.64
	width (cm)	3.5	6.42	5.85	6.47	5.54
Case 3	area (cm^2)	6.00	35.91	42.44	100.74	14.45
	width (cm)	1.0	6.13	6.91	8.68	2.76
Case 4	area (cm^2)	0.64	47.93	6.00	2.40	0.75
	width (cm)	0.39	1.13	1.11	1.17	0.47

one of the remaining 11 electrodes. This process was repeated using electrodes $\{1, 3, 5, 7, 9\}$ as the sink. For each current injection, voltage measurements between electrode 1 and the remaining 11 electrodes were taken. The data was computed using a FE mesh with 11815 nodes and 5824 triangular elements. Random additive Gaussian noise with standard deviation of 0.25% of the computed noiseless voltages was added to the data.

In the computation of the reconstructions, the conductivity was approximated in a first order piecewise linear basis with 932 nodes, i.e. the $\sigma \in \mathbb{R}^{932}$. The parameters a, b and c in the construction of Γ_σ (19) used in reconstructions (E1), (E2) and (E4) were set as $a = 15.15\text{mS}^2$, $b = 7.25\,\text{cm}$ and $c = 1.52 \times 10^{-2}\text{mS}^2$. As the expectation σ^* in (E2) and (E4), the best homogeneous conductivity estimate based on data set V_1 was used. The parameter α for the TV functional was selected as $\alpha = 0.25$. For the parameter β in the TV functional, we used value $\beta = 0.05$.

The standard difference reconstruction (E1) is shown in the bottom row in Fig 4. The reconstruction of the change $\delta\sigma$ is highly erroneous and has elongated artefacts towards the back of neck domain. These artefacts are due to the inhomogeneous background conductivity and the partial boundary problem where measurement electrodes are placed only at a small portion of the boundary. The reconstructions (E2) and (E3), which are based on computing separate absolute reconstructions of σ_1 and σ_2 are shown in the second and third row in Fig 4. Although the resolutions of reconstructions (E2) and (E3) are not very high, they are clearly better than (E1). Especially the reconstruction (E3) which uses TV regularization is quite feasible.

The reconstruction (E4) with the proposed approach is shown on the fourth row in Fig 4. This reconstruction clearly outperforms (E1)-(E3); especially, the size of the glottal opening has been reconstructed with a significantly better accuracy in (E4) than in the other estimates. The area and width estimates are given in Table 1. The width estimates were computed as the half widths of the reconstructed inclusions along a line cross-secting the glottis from the middle horizontally. The estimated width corresponding to reconstruction (E4) is 0.47 cm, which was relatively close to the true width 0.39 cm, while the other width estimates vary between 1.11 cm and 1.17 cm.

In this simulation, the electrodes were set only on the frontal part of the domain boundary that is close to the region-of-interest where the change of the target was known to take place. The results demonstrate that the ROI based reconstruction can tolerate well such a partial boundary setting: Indeed, although the background conductivity is rather complex, with small structures, reconstruction (E4) estimates

width of the glottis opening with less than 1 mm accuracy, which is a significant improvement to the resolution of the conventional reconstructions (E1)-(E3). This finding indicates that one could employ existing multichannel EGG measurement geometry (see e.q. [34]) for EIT imaging of vocal folds and therefore the ROI based reconstruction could allow flexibility in design of a practical measurement system.

6. **Conclusions.** In this paper, we proposed a novel approach to EIT image reconstruction in cases where EIT measurement of a time-varying target is available before and after a change of the target. In the proposed approach, the conductivity after the change is represented as a linear combination of the initial conductivity and the change, and the EIT inverse problem is formulated as simultaneous reconstruction of the initial conductivity and the change based on the two EIT data sets using the regularized least squares formalism. The approach enables the use of different spatial models for the initial conductivity and the change by different regularization functionals and it also allows for the restriction of the conductivity change to a region of interest in cases where the changes are *a priori* known to occur in a certain subvolume of the body.

The proposed approach was tested with three test cases using experimental data from laboratory set-up and one simulated test case related to EIT imaging of vocal folds. The proposed approach outperformed the conventional difference imaging approach and the frame-by-frame absolute imaging approach in all test cases. The findings suggest that the proposed approach can be useful in EIT applications where one is interested in detecting a change in the conductivity between two time instants, especially when the conductivity change can be restricted to a relatively small subdomain. The results of the simulation study also suggest that the approach can be particularly beneficial in partial boundary data problems.

In this study we computed results using 2D computational models. However, extension to 3D is straightforward. Furthermore, the proposed approach is based on solving the non-linear inverse problem, which is known to be prone to modelling errors, such as poorly known electrode locations, boundary shape and domain truncation. A few alternative methods for recovering from modeling errors exist, and combining those methods with the ROI reconstruction proposed in this paper is a relatively straightforward task.

Acknowledgments. The authors thank Mika Mikkola and Rami Korhonen from Department of Applied Physics, University of Eastern Finland, for their support with the MIMICS software in the glottis simulation.

REFERENCES

[1] A. P. Bagshaw, A. D. Liston, R. H. Bayford, A. Tizzard, A. P. Gibson, A. T. Tidswell, M. K. Sparkes, H. Dehghani, C. D. Binnie and D. S. Holder, Electrical impedance tomography of human brain function using reconstruction algorithms based on the finite element method, *Neuroimage*, **20** (2003), 752–764.

[2] J. Binette, M. Garon, P. Savard, M. McKee, M. Buschmann et al., Tetrapolar measurement of electrical conductivity and thickness of articular cartilage., *Journal of biomechanical engineering*, **126** (2004), 475–484.

[3] G. Boverman, T.-J. Kao, R. Kulkarni, B. S. Kim, D. Isaacson, G. J. Saulnier and J. C. Newell, Robust linearized image reconstruction for multifrequency EIT of the breast, *Medical Imaging, IEEE Transactions on*, **27** (2008), 1439–1448.

[4] A. Boyle, A. Adler and W. Lionheart, Shape deformation in two-dimensional electrical impedance tomography, *Medical Imaging, IEEE Transactions on*, **31** (2012), 2185–2193.

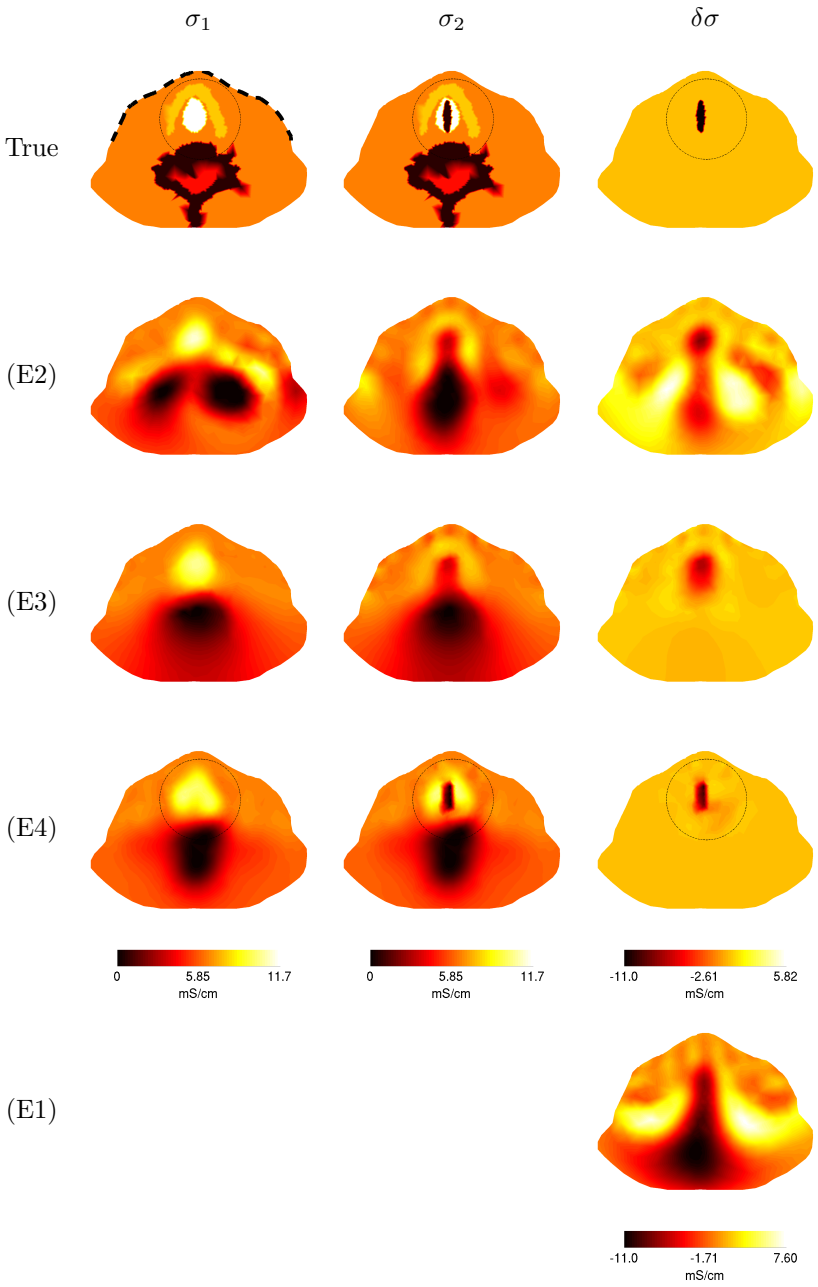

FIGURE 4. Case 4: Simulated test case of imaging of vocal folds. (E1)-(E4) refer to the estimates listed in section 4.2. The color scale denotes the common minimum to maximum scale of the conductivity values.

[5] B. Brown, Electrical impedance tomography (EIT): a review, *Journal of Medical Engineering & Technology*, **27** (2003), 97–108.

[6] M. Cheney, D. Isaacson and J. C. Newell, Electrical impedance tomography, *SIAM Rev*, **41** (1999), 85–101.
[7] K.-S. Cheng, D. Isaacson, J. Newell and D. G. Gisser, Electrode models for electric current computed tomography, *Biomedical Engineering, IEEE Transactions on*, **36** (1989), 918–924.
[8] V. Cherepenin, A. Karpov, A. Korjenevsky, V. Kornienko, Y. Kultiasov, M. Ochapkin, O. V. Trochanova and J. D. Meister, Three-dimensional EIT imaging of breast tissues: System design and clinical testing, *IEEE Trans. Med. Imag*, **21** (2002), 662–667.
[9] E. L. Costa, C. N. Chaves, S. Gomes, M. A. Beraldo, M. S. Volpe, M. R. Tucci, I. A. Schettino, S. H. Bohm, C. R. Carvalho, H. Tanaka et al., Real-time detection of pneumothorax using electrical impedance tomography*, *Critical care medicine*, **36** (2008), 1230–1238.
[10] E. L. Costa, R. G. Lima and M. B. Amato, Electrical impedance tomography, in *Intensive Care Medicine*, Springer, 2009, 394–404.
[11] W. Daily, A. Ramirez, D. LaBrecque and J. Nitano, Electrical resistivity tomography of vadose water movement, *Water. Resour. Res.*, **28** (1992), 1429–1442.
[12] J. Dardé, H. Hakula, N. Hyvönen and S. Staboulis, Fine-tuning electrode information in electrical impedance tomography, *Inverse Probl. Imaging*, **2012** (2012), 399–421.
[13] J. Dardé, N. Hyvönen, A. Seppänen and S. Staboulis, Simultaneous reconstruction of outer boundary shape and admittivity distribution in electrical impedance tomography, *SIAM Journal on Imaging Sciences*, **6** (2013), 176–198.
[14] J. Dardé, N. Hyvönen, A. Seppänen and S. Staboulis, Simultaneous recovery of admittivity and body shape in electrical impedance tomography: An experimental evaluation, *Inverse Problems*, **29** (2013), 085004.
[15] D. C. Dobson and F. Santosa, An image-enhancement technique for electrical impedance tomography, *Inverse problems*, **10** (1994), 317.
[16] A. V. Fiacco and G. P. McCormick, *Nonlinear programming: sequential unconstrained minimization techniques*, 4, Siam, 1990.
[17] A. Fourcin and E. Abberto, First application of a new laryngograph, *Med Biol Illustr*, **21** (1971), 172–182.
[18] I. Frerichs, J. Hinz, P. Herrmann, G. Weisser, G. Hahn, T. Dudykevych, M. Quintel and G. Hellige, Detection of local lung air content by electrical impedance tomography compared with electron beam CT, *Journal of applied physiology*, **93** (2002), 660–666.
[19] C. Gabriel, A. Peyman and E. Grant, Electrical conductivity of tissue at frequencies below 1 mhz, *Physics in medicine and biology*, **54** (2009), 4863.
[20] L. M. Heikkinen, T. Vilhunen, R. M. West and M. Vauhkonen, Simultaneous reconstruction of electrode contact impedances and internal electrical properties: Ii. laboratory experiments, *Measurement Science and Technology*, **13** (2002), 1855.
[21] T. Hézard, T. Hélie, B. Doval, N. Henrich and M. Kob, Non-invasive vocal-folds monitoring using electrical imaging methods, in *100 years of electrical imaging*, Paris, 2012.
[22] D. S. Holder, Electrical impedance tomography: Methods, history and applications, *Medical Physics*, **32** (2005), 2731.
[23] T. Hou, K. Loh and J. Lynch, Spatial conductivity mapping of carbon nanotube composite thin films by electrical impedance tomography for sensing applications, *Nanotechnology*, **18**.
[24] T. Hou and J. Lynch, Electrical impedance tomographic methods for sensing strain fields and crack damage in cementitious structures, *J. Intel. Mat. Syst. Str.*, **20** (2009), 1363–1379.
[25] D. Isaacson, J. L. Mueller, J. C. Newell and S. Siltanen, Reconstructions of chest phantoms by the D-bar method for electrical impedance tomography, *IEEE Transactions on Medical Imaging*, **23** (2004), 821–828.
[26] D. Isaacson, J. Mueller, J. Newell and S. Siltanen, Imaging cardiac activity by the D-bar method for electrical impedance tomography, *Physiological Measurement*, **27** (2006), S43–S50.
[27] B. Jin and P. Maass, Sparsity regularization for parameter identification problems, *Inverse Problems*, **28** (2012), 123001.
[28] J. P. Kaipio, V. Kolehmainen, E. Somersalo and M. Vauhkonen, Statistical inversion and monte carlo sampling methods in electrical impedance tomography, *Inverse problems*, **16** (2000), 1487.
[29] J. Kaipio, V. Kolehmainen, M. Vauhkonen and E. Somersalo, Inverse problems with structural prior information, *Inverse problems*, **15** (1999), 713.
[30] J. Kaipio and E. Somersalo, *Statistical and Computational Inverse Problems*, Springer New York, 2005.

[31] K. Karhunen, A. Seppänen, A. Lehikoinen, J. Blunt, J. Kaipio and J. Monteiro, Electrical resistance tomography for assessment of cracks in concrete, *ACI mater. J.*, **107** (2010), 523–531.
[32] K. Karhunen, A. Seppänen, A. Lehikoinen, P. Monteiro and J. Kaipio, Electrical resistance tomography imaging of concrete, *Cement Concrete Res.*, **40** (2010), 137–145.
[33] K. Knudsen, M. Lassas, J. Mueller and S. Siltanen, Regularized D-bar method for the inverse conductivity problem, *Inverse Problems and Imaging*, **3** (2009), 599–624.
[34] M. Kob and T. Frauenrath, A system for parallel measurement of glottis opening and larynx position, *Biomedical Signal Processing and Control*, **4** (2009), 221–228.
[35] V. Kolehmainen, M. Lassas and P. Ola, The inverse conductivity problem with an imperfectly known boundary, *SIAM Journal on Applied Mathematics*, **66** (2005), 365–383.
[36] V. Kolehmainen, M. Lassas and P. Ola, The inverse conductivity problem with an imperfectly known boundary in three dimensions, *SIAM Journal on Applied Mathematics*, **67** (2007), 1440–1452.
[37] V. Kolehmainen, M. Lassas and P. Ola, Electrical impedance tomography problem with inaccurately known boundary and contact impedances, *Medical Imaging, IEEE Transactions on*, **27** (2008), 1404–1414.
[38] J. Kourunen, T. Savolainen, A. Lehikoinen, M. Vauhkonen and L. Heikkinen, Suitability of a pxi platform for an electrical impedance tomography system, *Measurement Science and Technology*, **20** (2009), 015503.
[39] S. Leonhardt and B. Lachmann, Electrical impedance tomography: the holy grail of ventilation and perfusion monitoring?, *Intensive care medicine*, **38** (2012), 1917–1929.
[40] C. Lieberman, K. Willcox and O. Ghattas, Parameter and state model reduction for large-scale statistical inverse problems, *SIAM Journal on Scientific Computing*, **32** (2010), 2523–2542.
[41] S. Lindgren, H. Odenstedt, C. Olegård, S. Söndergaard, S. Lundin and O. Stenqvist, Regional lung derecruitment after endotracheal suction during volume-or pressure-controlled ventilation: a study using electric impedance tomography, *Intensive care medicine*, **33** (2007), 172–180.
[42] D. Liu, A. Seppänen, A. Nissinen, V. Kolehmainen, S. Siltanen and A.-M. Laukkanen, Preliminary results on 3D electrical impedance tomography imaging of vocal folds, in *8th International Conference on Voice Physiology and Biomechanics*, Erlangen, Germany, 2012.
[43] J. Mueller and S. Siltanen, *Linear and Nonlinear Inverse Problems with Practical Applications*, SIAM, 2012.
[44] A. Nissinen, L. Heikkinen, V. Kolehmainen and J. Kaipio, Compensation of errors due to discretization, domain truncation and unknown contact impedances in electrical impedance tomography, *Meas. Sci. Technol.*, **20** (2009), 105504 (13pp).
[45] A. Nissinen, V. Kolehmainen and J. P. Kaipio, Reconstruction of domain boundary and conductivity in electrical impedance tomography using the approximation error approach, *International Journal for Uncertainty Quantification*, **1**.
[46] A. Nissinen, V. P. Kolehmainen and J. P. Kaipio, Compensation of modelling errors due to unknown domain boundary in electrical impedance tomography, *Medical Imaging, IEEE Transactions on*, **30** (2011), 231–242.
[47] J. Nocedal and S. J. Wright, *Numerical optimization*, vol. 2, Springer New York, 1999.
[48] D. L. Phillips, A technique for the numerical solution of certain integral equations of the first kind, *J Assoc Comput Mach*, **9** (1962), 84–97.
[49] S. Pulletz, A. Adler, M. Kott, G. Elke, B. Gawelczyk, D. Schädler, G. Zick, N. Weiler and I. Frerichs, Regional lung opening and closing pressures in patients with acute lung injury, *Journal of Critical Care*, **27** (2012), 323–e11.
[50] M. Rothenberg, A multichannel electroglottograph, *Journal of Voice*, **6** (1992), 36–43.
[51] L. I. Rudin, S. Osher and E. Fatemi, Nonlinear total variation based noise removal algorithms, *Physica D: Nonlinear Phenomena*, **60** (1992), 259–268.
[52] D. Scott and H. McCann (eds.), *Handbook of Process Imaging for Automatic Control*, CRC Press, 2005.
[53] A. Seppänen, A. Nissinen, V. Kolehmainen, S. Siltanen and A. M. Laukkanen, Electrical impedance tomography imaging of larynx, in *Models and analysis of vocal emissions for biomedical applications, 7th International Workshop*, Firenze, Italy, 2011.
[54] A. Seppänen, M. Vauhkonen, P. Vauhkonen, E. Somersalo and J. Kaipio, State estimation with fluid dynamical evolution models in process tomography – an application to impedance tomography, *Inverse Problems*, **17** (2001), 467–483.

[55] S. Siltanen, J. Mueller and D. Isaacson, An implementation of the reconstruction algorithm of A. Nachman for the 2-D inverse conductivity problem, *Inverse Problems*, **16** (2000), 681–699.
[56] E. Somersalo, M. Cheney and D. Isaacson, Existence and uniqueness for electrode models for electric current computed tomography, *SIAM Journal on Applied Mathematics*, **52** (1992), 1023–1040.
[57] T. Tidswell, A. Gibson, R. H. Bayford and D. S. Holder, Three-dimensional electrical impedance tomography of human brain activity, *NeuroImage*, **13** (2001), 283–294.
[58] M. Vauhkonen, D. Vadasz, J. Kaipio, E. Somersalo and P. Karjalainen, Tikhonov regularization and prior information in electrical impedance tomography, *IEEE Trans Med Imaging*, **17** (1998), 285–293.
[59] P. Vauhkonen, *Image Reconstruction in Three-Dimensional Electrical Impedance Tomography*, PhD thesis, University of Kuopio, Kuopio, Finland, 2004.
[60] P. Vauhkonen, M. Vauhkonen, T. Savolainen and J. Kaipio, Three-dimensional electrical impedance tomography based on the complete electrode model, *IEEE Trans. Biomed. Eng*, **46** (1999), 1150–1160.
[61] J. A. Victorino, J. B. Borges, V. N. Okamoto, G. F. Matos, M. R. Tucci, M. P. Caramez, H. Tanaka, F. S. Sipmann, D. C. Santos, C. S. Barbas et al., Imbalances in regional lung ventilation a validation study on electrical impedance tomography, *American Journal of Respiratory and Critical Care Medicine*, **169** (2004), 791–800.
[62] T. Vilhunen, J. Kaipio, P. Vauhkonen, T. Savolainen and M. Vauhkonen, Simultaneous reconstruction of electrode contact impedances and internal electrical properties. Part I: Theory, *Meas. Sci. Technol.*, **13** (2002), 1848–1854.
[63] S. Wanjun, Y. Fusheng, Z. Wei, Z. Hongyi, F. Feng, S. Xuetao, L. Ruigang, X. Canhua, D. Xiuzhen and B. Tingyi, Image monitoring for an intraperitoneal bleeding model of pigs using electrical impedance tomography, *Physiological Measurement*, **29** (2008), 217.
[64] Y. Zou and Z. Guo, A review of electrical impedance techniques for breast cancer detection, *Medical engineering & physics*, **25** (2003), 79–90.

Received xxxx 20xx; revised xxxx 20xx.

E-mail address: dong.liu@uef.fi
E-mail address: ville.kolehmainen@uef.fi
E-mail address: samuli.siltanen@helsinki.fi
E-mail address: anne-maria.laukkanen@uta.fi
E-mail address: aku.seppanen@uef.fi